Measurement of Navier Slip on Individual Nanoparticles in Liquid

Jesse F. Collis,[†] Selim Olcum,[†] Debadi Chakraborty, Scott R. Manalis, and John E. Sader*

Read Online

ACCESS | Metrics & More | Article Recommendations | Supporting Information

ABSTRACT: The Navier slip condition describes the motion of a liquid relative to a neighboring solid surface, with its characteristic Navier slip length being a constitutive property of the solid−liquid interface. Measurement of this slip length is complicated by its small magnitude, expected to be in the nanometer range based on molecular simulations. Here, we report an experimental technique that interrogates the Navier slip length on individual nanoparticles immersed in liquid with subnanometer precision. Proof-of-principle experiments on individual, citrate-stabilized, gold nanoparticles in water give a constant slip length of 2.7 ± 0.6 nm (95% C.I.), independent of particle size. Achieving this feature of size independence is central to any measurement of this constitutive property, which is facilitated through the use of individual particles of varying radii. This demonstration motivates studies that can now validate the wealth of existing molecular simulation data on slip.
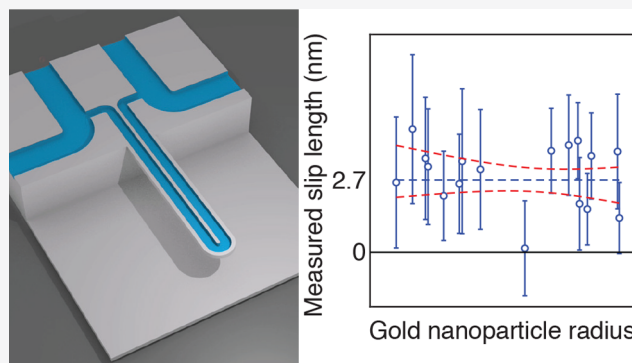
KEYWORDS: *liquid slippage, liquid/solid interfaces, suspended microchannel resonator, micro/nano fluid mechanics*

INTRODUCTION

The interaction of a liquid flowing past a solid surface has been studied extensively for the last century. It is now well accepted that the traditional no-slip boundary condition normally holds at large, macroscopic scales. Yet, use of the no-slip condition is being restricted with the increasing miniaturization of technology. Tremendous progress has been made in the last few decades toward understanding this situation using both molecular dynamics simulations[1−4] and high-resolution experimental techniques.[5−10]

Deviation from the no-slip boundary condition is described by the Navier slip condition[11−13]

$$[(\mathbf{u} - \mathbf{u}_s - b\mathbf{n}\cdot\mathbf{S})\cdot(\mathbf{I} - \mathbf{n}\mathbf{n})]_{\text{surface}} = 0 \qquad (1)$$

where $\mathbf{n}$ is the unit normal to the surface (into the liquid), $\mathbf{I}$ is the identity tensor, $\mathbf{u}$ and $\mathbf{u}_s$ are the liquid and solid velocity vectors, respectively, $\mathbf{S} \equiv 2\mathbf{e} = \nabla\mathbf{u} + (\nabla\mathbf{u})^{\text{T}}$ where $\mathbf{e}$ is the rate-of-strain tensor in the liquid and b is a proportionality constant: the "slip length". For a flat surface, b quantifies the depth of a hypothetical surface beneath the physical one where the no-slip condition would hold; see Figure 1a. Importantly, the Navier slip length is a constitutive property of the liquid−solid interface, i.e., it is independent of the flow geometry and its size.

Theoretical studies of slip in liquid are largely based on molecular dynamics simulations[1−4] and arguments from linear response theory.[14,15] There have also been suggestions that slip at the liquid−solid interface can be modeled as a kinetic rate process.[16,17] The key insight into come from molecular simulations is that, at low shear rates, the Navier slip condition

emerges, which depends sensitively on the properties of the interface.[8] Importantly, the wettability of the interface is observed in both molecular dynamics and linear response theory studies to affect the slip length. Interfaces with high wettability usually produce slip lengths of a few nanometers or less; conversely, interfaces with low wettability can have slip lengths in the tens of nanometers.[3] Given the slip length is a constitutive property of the liquid−solid interface (discussed above), these small slip lengths establish that slip is normally unimportant for flows at normal macroscopic length scales. That is, the no-slip condition can be used with confidence, apart from some important exceptions such as the moving three-phase contact line.[18]

On the experimental front, the degree of slip at the liquid−solid interface has been interrogated using a range of approaches including monitoring thermal fluctuations of free surfaces,[19] thermal motion of particle suspensions,[20] an array of particle velocimetry techniques,[21−24] atomic force microscope methodologies[25−29] through to use of the surface forces apparatus.[30] Large slip lengths (>1 μm) have mostly been attributed to dissolved gases on the solid surface.[7,9,31] For a review of nanofluidics, experiments used to measure slip at the liquid−solid interface and their findings, see refs 5−10 and 32.
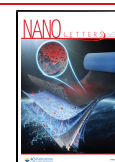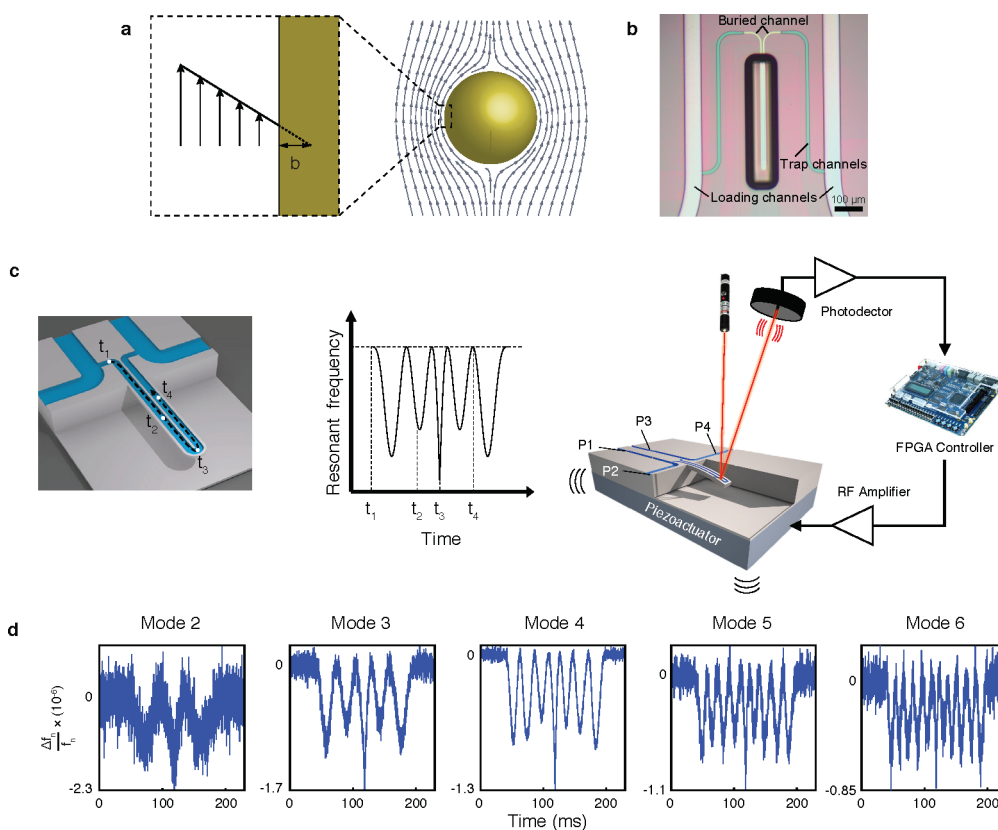
Figure 1. Schematic of SMR measurement protocol. (a) Streamlines of a liquid flowing past a sphere, which is moving with a steady velocity at zero Reynolds number (inertialess flow). Geometrically, the "slip length" is the extrapolated distance into the solid boundary where the no-slip boundary condition would apply (this interpretation holds exactly for a flat surface); see eq 1. (b) Optical micrograph of the SMR showing the cantilever enclosed in a vacuum chamber with an embedded microfluidic channel that is connected via loading, trap, and buried channels; nanoparticles are passed through these channels for measurement, one particle at a time. (c) [Left] Cross section of the SMR showing a U-shaped fluid channel embedded to the interior of the resonating cantilever. The dotted line represents the transit of a nanoparticle flowing through the SMR. The illustration shows time lapse snapshots of a single particle as it passes through the channel at times, $t_1 < t_2 < t_3 < t_4$. [Middle] Each negatively buoyant nanoparticle increases the inertial mass of the SMR, reducing the natural resonant frequencies of the SMR's flexural modes and therefore traces out the mode shapes (squared) of the SMR. A theoretical calculation of the resonant frequency of mode 3 versus time is shown here; the times, t_1 to t_4, correspond to particle positions labeled in the left subfigure. The magnitude of resonant frequency change depends both on the buoyant mass of the nanoparticle and the boundary condition at the nanoparticle surface; see eqs 2–4. [Right] An optical lever setup is used to convert the SMR tip motion to an electrical signal. An FPGA uses this signal to determine the drive signals for each of the modes using an array of digital phase-locked loop controllers. These drive signals are superposed and used to excite a piezo-ceramic actuator attached to the SMR chip. (d) Real measured (sample) data are shown for the resonant frequencies of each vibrational mode as a 126 nm radius gold nanoparticle passes through the SMR. A sample of data versus nanoparticle size is given in Figure S9.

Interestingly, confinement has also been observed to modify slip, with large slip lengths measured for liquid flows confined within carbon nanotubes.[6,33−35] Secchi et al.[35] reported a strong and systematic dependence of the measured slip length on tube diameter, $b = 300$ nm for a 15 nm radius tube and $b = 17$ nm for a (larger) 50 nm tube, in qualitative agreement with previous molecular simulations.[36,37] This shows that confinement can modify the above-mentioned constitutive nature of the slip length. The reported dependence is also affected by electrochemical properties of the liquid−solid interface, with no-slip being observed for boron nanotubes at all tube radii.[35]

Here, we develop an experimental technique to measure the Navier slip length on individual nanoparticles in liquid, with subnanometer precision, that does not involve confinement. This is achieved using a new modality of suspended microchannel resonators (SMRs)[38−43] that interrogates the hydrodynamic flow generated by a single nanoparticle in an unconfined liquid. The use of nanoparticles of different size enables the constitutive nature of the slip length to be examined and confirmed. This critical step ensures robust determination of the slip length, that can be compared to the vast library of molecular simulations of slip.[1−4] The developed technique is demonstrated in a proof-of-principle measurement using citrate-stabilized gold nanoparticles in water. This measurement is compared to available molecular simulations.

■ EXPERIMENTAL APPROACH

Measurement protocol. SMRs are cantilevered inertial mass sensors that allow ultrasensitive measurements—at the attogram level[41]—in liquid environments. This feature is central to the measurement of slip. An optical micrograph of the SMR used in this work is provided in Figure 1b, showing its (sensing) embedded microfluidic channel, which is fed via loading, trap, and buried channels; see Sections S1 and S2 for further details. The embedded, "U-shaped" channel is completely enclosed by the cantilever, which allows particles to flow through the device, as illustrated in Figure 1c. As a negatively buoyant, individual nanoparticle flows through the
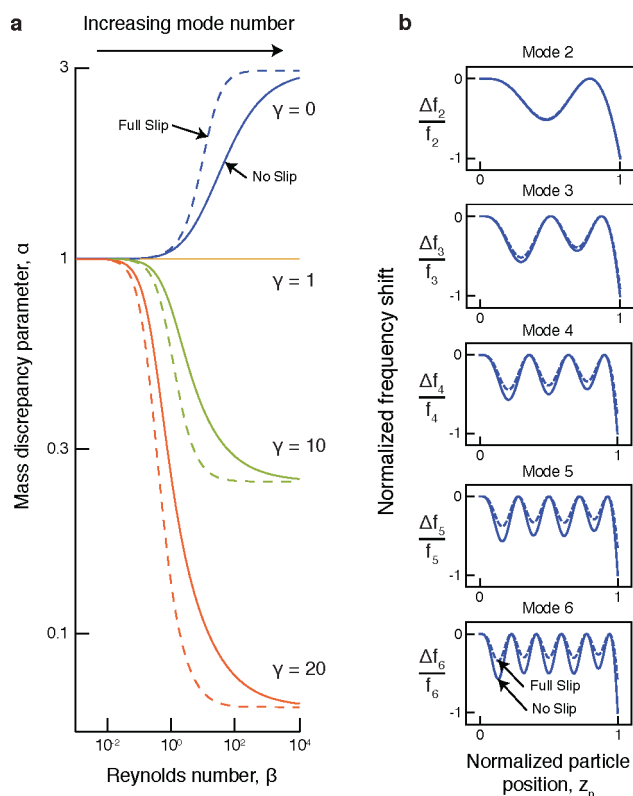
Figure 2. Effect of buoyant density ratio and slip length on the SMR frequency. (a) Mass discrepancy parameter, α, defined in eq 3, for a nanoparticle whose radius is far smaller than the SMR channel dimensions, as a function of the density ratio, γ, and oscillatory Reynolds number, β. No-slip at the particle's surface coincides with $\lambda \equiv b/R = 0$, (solid), whereas full slip, i.e., zero shear stress, at the particle's surface is given by $\lambda \to \infty$, (dashed). Equation 4 gives the analytical formula for α. In general, increasing slip reduces the effective size of the particle (by reducing drag), thereby reducing the observed buoyant mass. This explains the variation between the "No slip" and the "Full Slip" curves. (b) Theoretical frequency shifts for a particle with a density ratio of $\gamma = 20$ and an oscillatory Reynolds number for mode 2 of $\beta = 0.03$ (this corresponds to an ~150 nm radius gold nanoparticle in the present experiments). Frequency shifts are normalized by the maximum absolute value of the no-slip curve. Motion relative to the SMR is enhanced with increasing mode number (and hence frequency), causing a decrease in the observed buoyant mass of the particle (for particles more dense than the liquid). Slip increases this relative motion, causing a further decrease in the observed buoyant mass.

embedded channel of the SMR, it increases the inertial mass of the sensor. This reduces the natural resonant frequencies of the SMR's vibrational modes; Figure 1c, d show a theoretical calculation for mode 3 and actual measurements for modes 2−6, respectively. The nanoparticles remain suspended and do not sediment because of the action of Brownian forces.

Previous SMR measurements assume the particles move in concert with the surrounding liquid, enabling the true buoyant mass of the particle to be extracted. However, when buoyancy forces acting on the particle become large (by, for example, a large density imbalance between the particle and the liquid), the particle can move relative to the surrounding liquid, and the observed buoyant mass of the particle is no longer equal to its true buoyant mass.[43] In the present experiments, this motion is induced by using gold nanoparticles in water and by exciting the SMR's higher-order flexural modes, whose

resonant frequencies increase with mode order. Because this relative motion must drive a flow in the liquid, it is intimately connected to the hydrodynamic boundary condition at the particle's surface. This connection enables measurement of the Navier slip length through mass measurements on nanoparticles of different size.

Each individual nanoparticle is suspended in water and flows through the microfluidic channel of the SMR, which is simultaneously driven to oscillate at multiple vibrational modes spanning more than three octaves in frequency. A commensurate theoretical and statistical framework is developed, enabling the interpretation of these measurements on individual nanoparticles. Hundreds of measurements on each nanoparticle are collected by trapping the particle and flowing it back and forth through the SMR to mitigate the inherent frequency noise in the experiments and thus accurately and precisely determine the slip length of each nanoparticle. Thousands of measurements are performed in total; see Sections S3 and S4 for further details.

Theoretical framework. Mass measurements using inertial sensors relate the measured frequency shift of each vibration mode to an observed buoyant particle mass

$$\frac{\Delta f_n}{f_n} = -\frac{1}{2}\frac{M_P^{obs}}{M_{SMR}}U_n^2(z_p) \tag{2}$$

where $\omega_n = 2\pi f_n$ is the angular resonant frequency of the nth mode of the SMR without the particle, Δf_n is the resultant frequency shift in the presence of the particle, M_P^{obs} and M_{SMR} are the observed buoyant mass of the particle and the mass of the SMR, respectively, $U_n(z_p)$ is the scaled displacement mode shape of the SMR at the particle position, $z = z_p$, under the normalization $\int_0^L U_n^2(z)dz = L$, where L is the SMR's length; eq 2 holds provided $M_P^{obs} \ll M_{SMR}$. Particle motion relative to the SMR modifies the inertial mass of the system so that the observed buoyant particle mass is not the true buoyant mass of the particle. Use of eq 2 in such measurements then leads to a discrepancy relative to the true buoyant particle mass, which is quantified by the parameter

$$\alpha \equiv \frac{M_P^{obs}}{M_P^{true}} \tag{3}$$

where "obs" and "true" refer to the observed buoyant mass of the particle, calculated by application of eq 2, and the true buoyant mass of the particle, respectively. If there is no motion of the particle relative to the SMR, then $\alpha = 1$ and the true buoyant mass of the particle is recovered from eq 2.

An analytical formula is derived for α under the following assumptions: (i) the particle is a solid sphere, (ii) it is located far from any internal walls, (iii) its radius, R, is much smaller than the SMR length, L, and (iv) the particle oscillation amplitude is small relative to R; full details of the calculation are provided in Section S5. All assumptions are satisfied in the measurement, which is insensitive to particle nonsphericity (Section S6); analysis of the error induced by wall bounded flows is in Section S7. The key result is

$$\alpha = \frac{F(2 + \gamma) + 3(1 + 2\gamma)G}{F(1 + 2\gamma) + (1 + 2\gamma)^2 G} \tag{4}$$
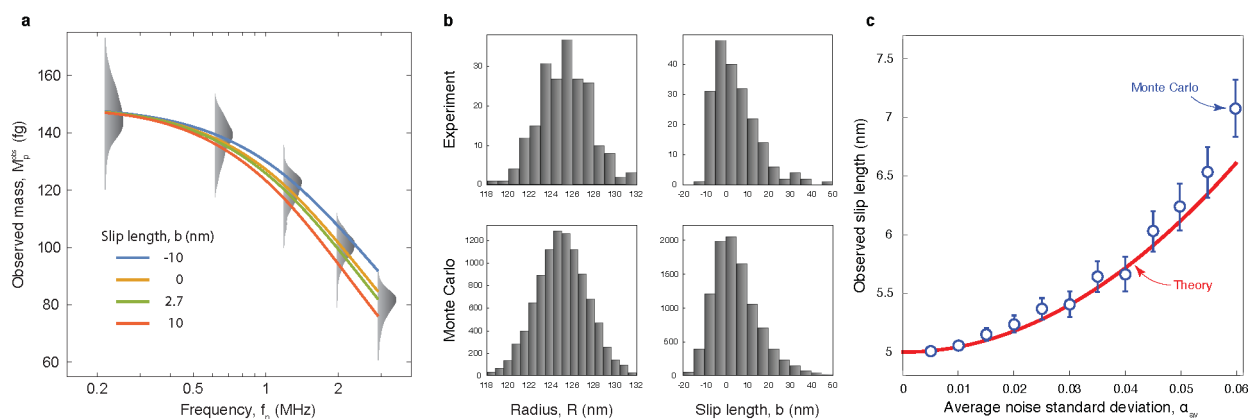
where

Figure 3. Measurement and simulations. (a) Observed mass, M_p^{obs}, vs frequency for 204 repeat measurements on a single gold nanoparticle (approximately 125 nm radius); theory for $M_p^{obs} \equiv \alpha M_p^{true}$ (curves) using eq 4 for different slip lengths (see legend). Distributions give density plots of the observed mass at each mode; spread is due to frequency noise. Curves give the theoretical prediction for the observed mass, as calculated from eq 3, for several different slip length values. (b) [Upper] *Measured* radii and slip lengths obtained from experiments for the same particle in panel a. [Lower] *Simulated* radii and slip lengths for a 125 nm radius gold nanoparticle with a nominal slip length of 5 nm. This differs slightly from Figure 4; however, varying this value has no qualitative effect on the simulated histograms; see Supplementary Section S8. Comparison to the measured histograms in panel a demonstrates that skewness in the fitted slip length distributions is a result of frequency noise; no frequency noise produces delta functions. (c) *Simulated* bias in the mean slip length as the frequency noise is varied in the system described in the caption to panel b; see Supplementary Section S8. The horizontal axis specifies the average standard deviation of the frequency noise over all modes, α_{av}. This coincides with the standard deviation of the mass discrepancy parameter because $\Delta f_n/f_n$ and α are related linearly; see eqs 2 and 3. Measurements in (a) yield $\alpha_{av} = 0.0401$. Solid (red) curve gives the theoretical mean of the slip length histogram as a function of frequency noise, using the derived asymptotic theory; see Supplementary Section S8.1. Dots (blue) are Monte Carlo simulations as described in the caption to panel b, with error bars specifying a 95% C.I.

$$F(x) = 81(1 + 2\lambda)^2 \left(1 + \sqrt{2\beta} + \beta + \frac{\sqrt{2}\,\beta^{3/2}x}{9} \right) \tag{5a}$$

$$G = (1 + 3\lambda)^2 \beta^2 + \sqrt{2}\,\lambda(1 + 3\lambda)\beta^{5/2} + \lambda^2 \beta^3 \tag{5b}$$

Here, $\beta \equiv \omega_n R^2 \rho_f/\mu$ is the oscillatory Reynolds number and $\gamma \equiv \rho_p/\rho_f$ is the particle-to-liquid density ratio, where R is the particle radius, ρ_p is the particle density, ρ_f is the liquid density and μ is the liquid's shear viscosity. The nondimensional slip length, $\lambda \equiv b/R$, is scaled by the particle radius. The combination of eqs 2–4 fully connect the measured frequency shift to (i) the particle radius and (ii) the slip length, the primary variables to be measured.

Figure 2a provides theoretical results for the mass discrepancy parameter, α, as a function of the oscillatory Reynolds number, β, for a range of density ratios, γ. Bounding values for the nondimensional slip length, $\lambda \rightarrow 0$ and ∞, are also given, corresponding to no-slip and zero shear stress (full slip) at the solid surface, respectively; see eq 1. In the limit where the particle density approaches that of the liquid, i.e., $\gamma \rightarrow 1$, the true buoyant particle mass is recovered with $\alpha = 1$. Figure 2a also reveals that slip can only affect the measurement for intermediate values of β, a key requirement in designing the present measurement of slip.

Figure 2b shows theoretical calculations of the frequency shift for each vibration mode of the SMR used in this study. This highlights the effects of slip for a 150 nm gold nanoparticle passing through the SMR. By fitting such theoretical results to the corresponding measured frequency shift curves (as in Figure 1d), the radius and slip length of each nanoparticle can be determined; the required procedure is detailed below.

■ RESULTS AND DISCUSSION

We now report the results of proof-of-principle measurements demonstrating the proposed method to measure the Navier slip length. This includes a detailed analysis of the measurements and the required data processing to extract the Navier slip length of individual nanoparticles.

Measurements on Single Nanoparticles. Gold nanoparticles with identical surface treatment but different sizes are used (Section S4). All nanoparticles are chosen to span the above-mentioned intermediate β-range, using SMR vibrational modes 2–6. On each pass through the SMR, a frequency shift versus particle position curve is measured for each of the five SMR vibrational modes. Fitting each of these curves to eq 2 gives an observed buoyant mass, one for each of the excited vibrational SMR modes (Section S3).

These five measurements of observed buoyant mass versus vibrational mode frequency give experimental counterparts (Figure 3a) to the theoretical curves in Figure 2a. Fitting eq 4 to these measured curves, using a least-squares fitting procedure, produces a single radius and a single slip length (Section S3). Because the expected slip lengths are much smaller than the particle radius, the resulting effect of slip on the frequency shift curves is very small. To overcome this difficulty, the measurement process is repeated hundreds of times on each particle—providing histograms of the measured radius and slip length.

Histograms of the measured radii of individual particles, from repeat measurements, appear to be normally distributed with small variance, see Figure 3b. This distribution is consistent with the central limit theorem, and as such, the average of these measured distributions should provide the true particle radius—small bias exists that is negligible relative to the observed standard error; see Figure S6.

In contrast to the measured radii, however, histograms of the measured slip lengths display a distinct right skewness with
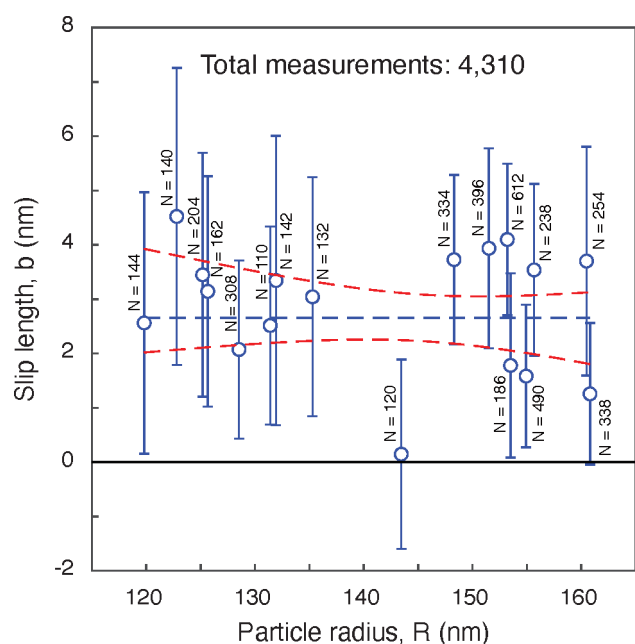
Figure 4. Measured Navier slip length versus nanoparticle radius for 17 individual gold nanoparticles of different radii; the full particle size range accessible using the present SMR is shown. The complete data set of 22 particles measured, including smaller and larger particles (radii 67.9−205.0 nm) excluded for unacceptable signal-to-noise (Section S10) or wall effects (see Section S7), is given in Figure S4a. Linear regression fit to the measured slip lengths of the remaining 17 particles versus their radii (119.8−160.8 nm)—shown here—is performed; this fit is weighted by the inverse squares of the standard error of each slip length measurement. Red dashed (curved) bands define two standard errors for straight lines of varying slope that fit the data. The blue dashed horizontal line (zero slope) is the best fit to a constant slip length. The solid black horizontal line corresponds to no-slip—it is provided for reference. Error bars specify a 95% C.I., with uncertainties in the particle radii being smaller than the size of the data points.

large variance, see Figure 3b. To robustly measure the actual slip length, i.e., without the convoluting effects of measurement noise, we investigate the origin of this difference in histograms for the particle radius and slip length, on a single particle. This is achieved using Monte Carlo simulations of the measurements that involve numerically synthesized data and incorporate frequency noise levels observed in measurements; see Section S8. Simulations corresponding to measurements in Figure 3b [upper] are reported in Figure 3b [lower] and bear a striking resemblance. This shows that the observed skewness is a direct result of frequency noise and immediately suggests that skewness in the slip length histograms can be deconvoluted to recover the actual slip length. A theoretical analysis is performed on the fitting procedure to connect the observed slip lengths to the actual slip length; see Section S8.1. Figure 3c gives the results of this analysis by showing the mean of the slip length histogram versus the standard deviation in the frequency noise (averaged over all measured SMR modes). The derived theory independently predicts the Monte Carlo simulations and enables the actual slip length to be determined.

Particles of radii in the range 115 to 165 nm are used, because particles of smaller size exhibit unacceptable signal-to-noise (frequency shift signal is proportional to radius cubed) while those of larger size are affected by the bounding walls of

the SMR used in this study. See Figure S4a for the full data set including those particles excluded for the reasons stated above.

The synthesis process for the gold nanoparticles results in deviations from sphericity. The effect of this nonsphericity is fully characterized using both analytical and numerical calculations, alongside TEM images of the nanoparticles; see Section S6. The developed protocol is insensitive to particle nonsphericity that results in a negative slip length bias that is much smaller than, and therefore cannot account for, the measured positive slip length. This bias is one order of magnitude smaller than the reported slip lengths and well within the reported 95% confidence intervals.

Measured Navier Slip Length. Figure 4 reports data for the actual slip length of each nanoparticle—taken from hundreds of individual measurements—and their associated uncertainties (95% C.I.). This data set evidently displays an average slip length, over all nanoparticles, which is nonzero and positive. A statistical analysis using linear regression of the slip length data set in Figure 4, weighted by the inverse of the standard errors squared, is performed to assess the independence of the slip length on the particle radius. This shows that there is no evidence for a correlation between radius and measured slip length; see Section S9.

A regression fit using a constant term only is then applied and yields a slip length of 2.7 ± 0.6 nm (95% C.I. with a p-value less than 1×10^{-6}). That is, a nonzero (and positive) slip length of approximately ten molecular diameters of water is accurately measured. We thus conclude that the reported measurements of slip length, on individual particles of different size, are consistent with the constitutive property of the Navier slip condition: the slip length is independent of the particle, and its size, for the same solid material and liquid.

An upper bound for the liquid shear rate at the particle surface, encountered in measurements, is $1 \times 10^5 \text{ s}^{-1}$. Molecular simulations show that nonlinearities in slip occur at shear rates at least 3 orders-of-magnitude larger.[44] Molecular simulations[3] also show that the slip length increases with the degree of hydrophobicity—no-slip occurs for hydrophilic surfaces and a slip length of no more than 20 nm arises for highly hydrophobic surfaces (contact angles of approximately 140°). Recent experiments[45] show that citrate-stabilized gold nanoparticle surfaces used in this study are weakly hydrophobic with a contact angle in water of about 95°. The measured slip length of 2.7 ± 0.6 nm in this study on individual (weakly hydrophobic) citrate stabilized gold nanoparticles is compatible with molecular simulation data for this level of hydrophobicity; see Figure 3 of ref 3.

■ CONCLUSIONS AND FUTURE DIRECTIONS

The uniqueness of this work lies in the ability to measure the Navier slip length of an individual nanoparticle in an unconfined liquid, with subnanometer precision, while directly probing its constitutive nature. This experimental development, its associated theoretical framework, and the proof-of-principle demonstration on citrate-stabilized gold nanoparticles in water, enable studies of other nanoparticle systems that can be used to validate the wealth of molecular simulation data on slip.

This development can be used to experimentally connect the particle surface and liquid properties to the resulting slip length. Future measurements could explore the effects of particle wettability, particle crystal structure, particle surface functionalization, particle surface charge, system temperature,

liquid viscosity, and polarity. An array of practically realizable experiments are reported in Table S4. These are based on two previously validated SMR devices, which facilitates their implementation.

■ ASSOCIATED CONTENT

Ⓢ Supporting Information

■ AUTHOR INFORMATION

Corresponding Author

John E. Sader − ARC Centre of Excellence in Exciton Science, School of Mathematics and Statistics, The University of Melbourne, Victoria 3010, Australia; ⓞ orcid.org/0000-0002-7096-0627; Email: jsader@unimelb.edu.au

Authors

Jesse F. Collis − ARC Centre of Excellence in Exciton Science, School of Mathematics and Statistics, The University of Melbourne, Victoria 3010, Australia; ⓞ orcid.org/0000-0003-0992-101X

Selim Olcum − Koch Institute for Integrative Cancer Research, Massachusetts Institute of Technology, Cambridge, Massachusetts 02139, United States

Debadi Chakraborty − ARC Centre of Excellence in Exciton Science, School of Mathematics and Statistics, The University of Melbourne, Victoria 3010, Australia

Scott R. Manalis − Koch Institute for Integrative Cancer Research, Massachusetts Institute of Technology, Cambridge, Massachusetts 02139, United States; Department of Biological Engineering and Department of Mechanical Engineering, Massachusetts Institute of Technology, Cambridge, Massachusetts 02139, United States

Complete contact information is available at:
https://pubs.acs.org/10.1021/acs.nanolett.1c00603

Author Contributions

[†]J.F.C. and S.O. contributed equally to this work.

Notes

The authors declare the following competing financial interest(s): S.R.M. is a co-founder of Travera and Affinity Biosensors, which develops technologies relevant to the research presented in this work.

■ ACKNOWLEDGMENTS

■ REFERENCES

(1) Thompson, P. A.; Troian, S. M. A general boundary condition for liquid flow at solid surfaces. *Nature* **1997**, *389*, 360−362.

(2) Barrat, J. L.; Bocquet, L. Large slip effect at a nonwetting fluid-solid interface. *Phys. Rev. Lett.* **1999**, *82*, 4671−4674.

(3) Huang, D. M.; Sendner, C.; Horinek, D.; Netz, R. R.; Bocquet, L. Water slippage versus contact angle: A quasiuniversal relationship. *Phys. Rev. Lett.* **2008**, *101*, 226101.

(4) Voronov, R. S.; Papavassiliou, D. V.; Lee, L. L. Review of fluid slip over superhydrophobic surfaces and its dependence on the contact angle. *Ind. Eng. Chem. Res.* **2008**, *47*, 2455−2477.

(5) Neto, C.; Evans, D. R.; Bonaccurso, E.; Butt, H. J.; Craig, V. S. Boundary slip in Newtonian liquids: A review of experimental studies. *Rep. Prog. Phys.* **2005**, *68*, 2859−2897.

(6) Whitby, M.; Quirke, N. Fluid flow in carbon nanotubes and nanopipes. *Nat. Nanotechnol.* **2007**, *2*, 87−94.

(7) Lauga, E.; Brenner, M. P.; Stone, H. A. Microfluidics: The No-Slip Boundary Condition In *Springer Handbook of Experimental Fluid Mechanics*; Tropea, C., Foss, J. F., Yarin, A. L., Eds.; Springer: Heidelberg, Germany, 2007; pp 1219−1240.

(8) Bocquet, L.; Charlaix, E. Nanofluidics, from bulk to interfaces. *Chem. Soc. Rev.* **2010**, *39*, 1073−1095.

(9) Shu, J. J.; Bin Melvin Teo, J.; Kong Chan, W. Fluid velocity slip and temperature jump at a solid surface. *Appl. Mech. Rev.* **2017**, *69*, 020801.

(10) Bocquet, L. Nanofluidics coming of age. *Nat. Mater.* **2020**, *19*, 254−256.

(11) Maxwell, J. C. On stresses in rarefied gases arising from inequalities of temperature. *Proc. R. Soc. London* **1878**, *27*, 304−308.

(12) Vincenti, W. G.; Kruger, C. H. J. *Introduction to Physical Gas Dynamics*, 2nd ed.; John Wiley & Sons: New York, 1967.

(13) Cercignani, C. *Mathematical Methods in Kinetic Theory*, 2nd ed.; Springer Science & Business Media: New York, 1969.

(14) Bocquet, L.; Barrat, J. L. On the Green−Kubo relationship for the liquid-solid friction coefficient. *J. Chem. Phys.* **2013**, *139*, 044704.

(15) Huang, K.; Szlufarska, I. Green−Kubo relation for friction at liquid-solid interfaces. *Physical Review E - Statistical, Nonlinear, and Soft Matter Physics* **2014**, *89*, 032119.

(16) Lichter, S.; Martini, A.; Snurr, R. Q.; Wang, Q. Liquid slip in nanoscale channels as a rate process. *Phys. Rev. Lett.* **2007**, *98*, 226001.

(17) Wang, G. J.; Hadjiconstantinou, N. G. Universal molecular-kinetic scaling relation for slip of a simple fluid at a solid boundary. *Physical Review Fluids* **2019**, *4*, 1−10.

(18) Snoeijer, J. H.; Andreotti, B. Moving contact lines: Scales, regimes, and dynamical transitions. *Annu. Rev. Fluid Mech.* **2013**, *45*, 269−292.

(19) Pottier, B.; Frétigny, C.; Talini, L. Boundary Condition in Liquid Thin Films Revealed through the Thermal Fluctuations of Their Free Surfaces. *Phys. Rev. Lett.* **2015**, *114*, 227801.

(20) Joly, L.; Ybert, C.; Bocquet, L. Probing the nanohydrodynamics at liquid-solid interfaces using thermal motion. *Phys. Rev. Lett.* **2006**, *96*, 046101.

(21) Bouzigues, C. I.; Tabeling, P.; Bocquet, L. Nanofluidics in the debye layer at hydrophilic and hydrophobic surfaces. *Phys. Rev. Lett.* **2008**, *101*, 114503.

(22) Lasne, D.; Maali, A.; Amarouchene, Y.; Cognet, L.; Lounis, B.; Kellay, H. Velocity profiles of water flowing past solid glass surfaces using fluorescent nanoparticles and molecules as velocity probes. *Phys. Rev. Lett.* **2008**, *100*, 214502.

(23) Li, H.; Yoda, M. An experimental study of slip considering the effects of non-uniform colloidal tracer distributions. *J. Fluid Mech.* **2010**, *662*, 269−287.

(24) Li, Z.; D'Eramo, L.; Lee, C.; Monti, F.; Yonger, M.; Tabeling, P.; Chollet, B.; Bresson, B.; Tran, Y. Near-wall nanovelocimetry based on total internal reflection fluorescence with continuous tracking. *J. Fluid Mech.* **2015**, *766*, 147−171.

(25) Bonaccurso, E.; Butt, H. J.; Craig, V. S. Surface Roughness and Hydrodynamic Boundary Slip of a Newtonian Fluid in a Completely Wetting System. *Phys. Rev. Lett.* **2003**, *90*, 4.

(26) Honig, C. D.; Ducker, W. A. No-slip hydrodynamic boundary condition for hydrophilic particles. *Phys. Rev. Lett.* **2007**, *98*, 028305.

(27) Maali, A.; Cohen-Bouhacina, T.; Kellay, H. Measurement of the slip length of water flow on graphite surface. *Appl. Phys. Lett.* **2008**, *92*, 053101.

(28) Guriyanova, S.; Semin, B.; Rodrigues, T. S.; Butt, H. J.; Bonaccurso, E. Hydrodynamic drainage force in a highly confined geometry: Role of surface roughness on different length scales. *Microfluid. Nanofluid.* **2010**, *8*, 653−663.

(29) Henry, C. L.; Craig, V. S. Measurement of no-slip and slip boundary conditions in confined Newtonian fluids using atomic force microscopy. *Phys. Chem. Chem. Phys.* **2009**, *11*, 9514−9521.

(30) Cottin-Bizonne, C.; Steinberger, A.; Cross, B.; Raccurt, O.; Charlaix, E. Nanohydrodynamics: The intrinsic flow boundary condition on smooth surfaces. *Langmuir* **2008**, *24*, 1165−1172.

(31) De Gennes, P. G. On fluid/wall slippage. *Langmuir* **2002**, *18*, 3413−3414.

(32) Zhu, L.; Attard, P.; Neto, C. Reconciling slip measurements in symmetric and asymmetric systems. *Langmuir* **2012**, *28*, 7768−7774.

(33) Majumder, M.; Chopra, N.; Andrews, R.; Hinds, B. J. Enhanced flow in carbon nanotubes. *Nature* **2005**, *438*, 44−44.

(34) Radha, B.; et al. Molecular transport through capillaries made with atomic-scale precision. *Nature* **2016**, *538*, 222−225.

(35) Secchi, E.; Marbach, S.; Niguès, A.; Stein, D.; Siria, A.; Bocquet, L. Massive radius-dependent flow slippage in carbon nanotubes. *Nature* **2016**, *537*, 210−213.

(36) Thomas, J. A.; McGaughey, A. J. Water flow in carbon nanotubes: Transition to subcontinuum transport. *Phys. Rev. Lett.* **2009**, *102*, 184502.

(37) Kannam, S. K.; Todd, B. D.; Hansen, J. S.; Daivis, P. J. How fast does water flow in carbon nanotubes? *J. Chem. Phys.* **2013**, *138*, 094701.

(38) Burg, T. P.; Godin, M.; Knudsen, S. M.; Shen, W.; Carlson, G.; Foster, J. S.; Babcock, K.; Manalis, S. R. Weighing of biomolecules, single cells and single nanoparticles in fluid. *Nature* **2007**, *446*, 1066−1069.

(39) Dohn, S.; Svendsen, W.; Boisen, A.; Hansen, O. Mass and position determination of attached particles on cantilever based mass sensors. *Rev. Sci. Instrum.* **2007**, *78*, 103303.

(40) Lee, J.; Shen, W.; Payer, K.; Burg, T. P.; Manalis, S. R. Toward attogram mass measurements in solution with suspended nanochannel resonators. *Nano Lett.* **2010**, *10*, 2537−2542.

(41) Olcum, S.; Cermak, N.; Wasserman, S. C.; Christine, K. S.; Atsumi, H.; Payer, K. R.; Shen, W.; Lee, J.; Belcher, A. M.; Bhatia, S. N.; Manalis, S. R. Weighing nanoparticles in solution at the attogram scale. *Proc. Natl. Acad. Sci. U. S. A.* **2014**, *111*, 1310−1315.

(42) Olcum, S.; Cermak, N.; Wasserman, S. C.; Manalis, S. R. High-speed multiple-mode mass-sensing resolves dynamic nanoscale mass distributions. *Nat. Commun.* **2015**, *6*, 1−8.

(43) Yan, H.; Zhang, W. M.; Jiang, H. M.; Hu, K. M.; Hong, F. J.; Peng, Z. K.; Meng, G. A measurement criterion for accurate mass detection using vibrating suspended microchannel resonators. *Journal of Sound and Vibration* **2017**, *403*, 1−20.

(44) Bocquet, L.; Barrat, J. L. Flow boundary conditions from nano-to micro-scales. *Soft Matter* **2007**, *3*, 685−693.

(45) Valsesia, A.; Desmet, C.; Ojea-Jiménez, I.; Oddo, A.; Capomaccio, R.; Rossi, F.; Colpo, P. Direct quantification of nanoparticle surface hydrophobicity. *Communications Chemistry* **2018**, *1*, 53.